Journal of
Materials Chemistry A

Materials for energy and sustainability

Accepted Manuscript

This article can be cited before page numbers have been issued, to do this please use: A. P. Nedumthuruthiyil, A. Rajendran, D. Dhiman, B. Pavithra, T. Ghatak, B. Saha, K. Singh, S. Ghosh and A. Sarbajna, *J. Mater. Chem. A*, 2026, DOI: 10.1039/D6TA02884E.

ROYAL SOCIETY OF CHEMISTRY

rsc.li/materials-a

View Article Online
DOI: 10.1039/D6TA02884E

ARTICLE

Divergence Between Activity Metrics and Mechanistic Interpretability in Anchored Molecular Electrocatalysts

Received 00th January 20xx,
Accepted 00th January 20xx

DOI: 10.1039/x0xx00000x

Akash Philip Nedumthuruthiyil,†[a] Akhil Rajendran,[a] Dhruv Dhiman,[a] Pavithra B,[a,b] Tapas Ghatak,[a] Biswajit Saha,[c] Kuldeep Singh,[d] Sreetama Ghosh[b*] and Abir Sarbajna[a*]

Anchoring molecular electrocatalysts to conductive supports can preserve nominal molecular identity while modifying interfacial behaviour. As a result, commonly reported activity metrics do not necessarily reflect the operative molecular state after immobilization. Here, we analyse 157 reported base-metal systems spanning hydrogen evolution, oxygen evolution, and photoelectrochemical reactions to examine how catalytic activity relates to interfacial effects and the completeness of reported characterization. In this analysis, mechanistic interpretability refers to how strongly the reported evidence supports assignment of measured activity to the molecular or molecularly derived active site, rather than to reconstruction, decomposition, leaching, support-derived activity, transport effects, or photophysical losses. We evaluate this by separating mechanistic utility, interfacial penalty, and evidence completeness within a fixed U–R descriptor framework. The analysis shows that systems with similar electrochemical performance can differ substantially in mechanistic interpretability. These variations are associated with anchoring-induced perturbations and the completeness of reported characterization. The trends are observed across reductive, oxidative, and photochemical regimes. This work provides a practical basis for evaluating when reported activity can be more strongly associated with molecular-level behaviour in anchored electrocatalysts.

1. Introduction

Anchoring molecular electrocatalysts to conductive supports has become a key approach that can translate the chemical tunability of coordination complexes into operationally robust electrochemical and photoelectrochemical systems.[1] Molecular catalysts offer tunability of ligand environment, metal identity, redox properties, proton relays, and, in many cases, extended secondary-sphere effects, which are often difficult to systematically engineer in extended solids.[2] Anchoring these molecules to electrodes allows coupling molecular reactivity with solid supports, positioning them at the interface between homogeneous catalysis and heterogeneous electrochemistry.[3] Under immobilized conditions, electron transfer is governed by the conductive support and proton delivery by the electrolyte, while solvation, electric fields, and mass transport differ from bulk solution. As a result, anchored molecular catalysts constitute a chemically distinct class of interfacial catalytic systems rather than a simple hybrid of existing approaches (Fig. 1a).[4,5]

Molecular catalysts have been immobilized using various strategies reported across the literature, such as covalent grafting, physisorption, π–π interactions, and supramolecular, interfacial, or hybrid architectures (Fig. 1b).[6] Differences in electronic interaction with the support, molecular flexibility, and the tendency to reorganize or degrade under (photo)electrochemical conditions make mechanistic interpretation difficult, yet these factors are often not explicitly considered in how anchored molecular electrocatalysts are assessed.[7] These effects may involve changes in electron transfer through the support, restricted access to the active site, aggregation of molecules on the surface, or changes in the ligand sphere during operation. Some of the most important cases, such as ligand exchange, partial metal loss, surface reconstruction, or local pH/transport effects, are also among the easiest to miss because they may not be obvious from activity data alone. We therefore define mechanistic interpretability as the extent to which the reported evidence supports assigning the measured activity to a molecular or molecularly derived active site, without assuming that the original molecular structure is retained during operation. Performance metrics such as overpotential, Tafel slope, and current density remain central for benchmarking, yet in anchored systems these responses frequently conflate molecular chemistry with interfacial transport, structural evolution, and local environment.[8] As a result, similar electrochemical responses may originate from different

[a] Advanced Catalysis Facility, Department of Chemistry, School of Advanced Sciences, Vellore Institute of Technology, Vellore 632014, Tamil Nadu, India
[b] CO_2 Research and Green Technologies Centre, Vellore Institute of Technology, Vellore 632014, Tamil Nadu, India
[c] Materials Science Group, Coal Energy and Materials Sciences Division, CSIR-North East Institute of Science and Technology, Jorhat, Assam 785006, India
[d] Makromolekulare Chemie, Universität Bayreuth, Universitätsstraße 30, 95447 Bayreuth, Germany
† These authors contributed equally.

View Article Online
DOI: 10.1039/D6TA02884E

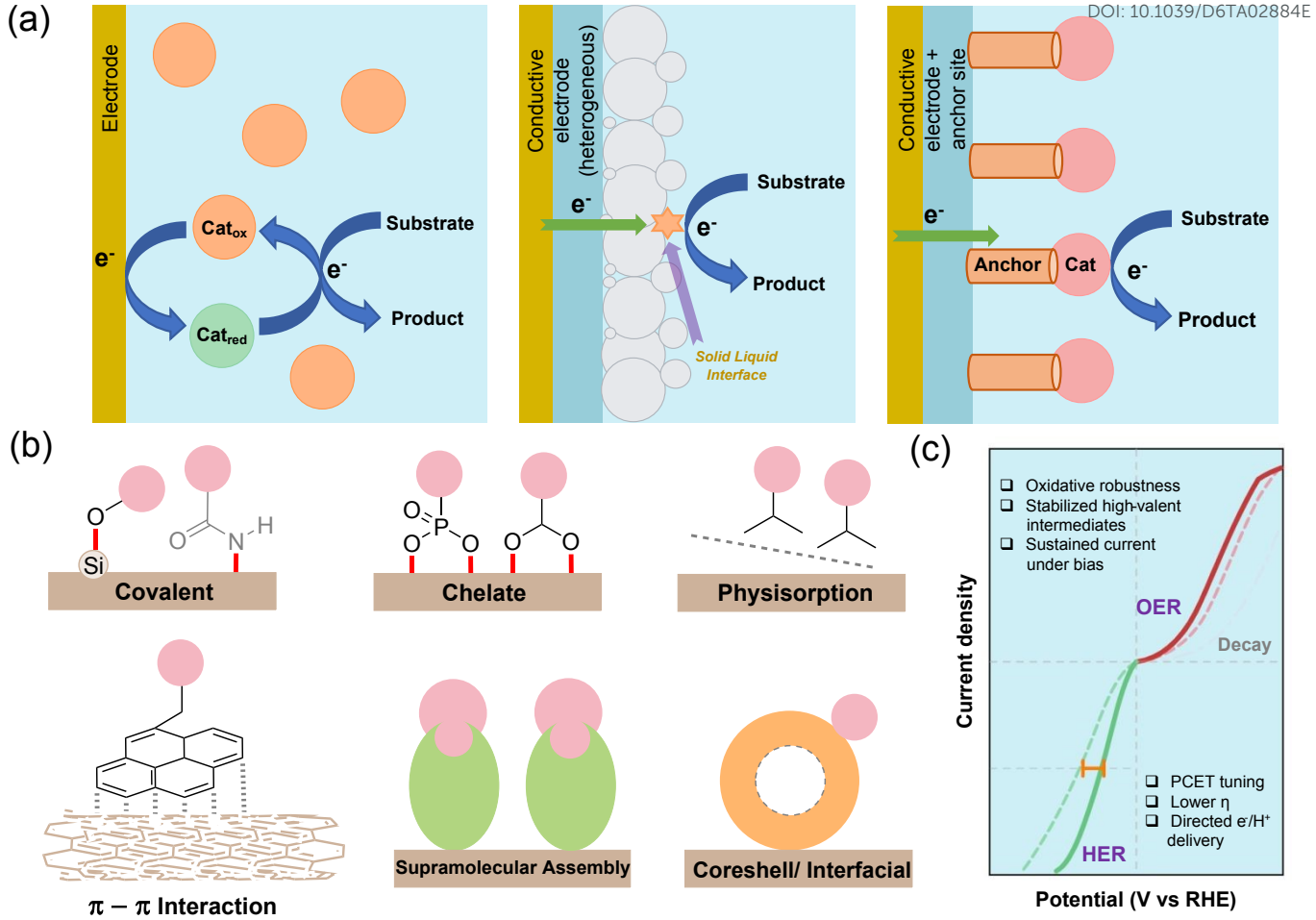

Fig. 1 Conceptual positioning of anchored molecular electrocatalysts (a) Homogeneous, heterogeneous, and anchored electrocatalytic systems compared schematically. (b) Anchoring interactions used to immobilize molecular catalysts on conductive supports, such as covalent attachment, chelation, physisorption, π–π interactions, supramolecular assembly, and core–shell or interfacial architectures. (c) Schematic current–potential curves for anchored (solid) and unanchored (dashed) systems during HER and OER.

underlying interfacial states.[9] This ambiguity is especially pronounced for hydrogen and oxygen evolution reactions, where interfacial charge transfer and oxidative stress strongly influence catalyst behaviour after immobilization (Fig. 1c).[10]

These issues become apparent from a recent systematic survey of anchored molecular electrocatalysts, in which we surveyed and categorized a broad range of base-metal systems reported for hydrogen evolution and oxygen evolution reactions.[11] While the report highlighted the diversity of ligands, anchoring strategies, supports, and operating conditions across the field, it also revealed the absence of a chemically consistent basis for comparing mechanistic claims across studies. Mechanistic assignments for anchored catalysts are usually system-specific and do not automatically generalize across different studies because the quality and depth of supporting evidence in the literature differ substantially.[12] As a result, the literature contains many apparent contradictions that cannot be resolved by performance metrics alone.[13]

In this work, we analyse intrinsic catalytic features alongside limitations introduced by anchoring and assess the completeness of supporting evidence using fixed criteria. We define mechanistic utility (Utility Descriptor Potentials, U) as intrinsic molecular features that enable catalytic pathways and mechanistic penalty (Rate and Stability Determining Limitations, R) as limitations arising from immobilization and interfacial constraints. Across 157 anchored molecular electrocatalysts covering hydrogen evolution (HER), oxygen evolution (OER), photoelectrochemical hydrogen evolution (PEC-HER), and photoelectrochemical oxygen evolution (PEC-OER), the systems are observed to cluster along a diagonal utility–penalty trend. This analysis provides a structured basis for evaluating when reported activity is supported by molecular-level evidence in anchored electrocatalysts.

2. Methods

We analysed 157 anchored molecular electrocatalysts reported for HER, OER, and related photoelectrochemical reactions. For each system, catalyst identity, anchoring mode, reaction assignment, experimental conditions, reported activity metrics, and qualitative mechanistic evidence were extracted from the literature using predefined extraction rules. Mechanistic interpretability was treated as an evidence-supported attribution problem, rather than as direct proof of the operative active site. Mechanistic tendencies, mechanistic utility, interfacial penalty, and evidence completeness were

View Article Online DOI: 10.1039/D6TA02884F

represented using bounded, rule-based descriptors that were fixed prior to aggregation. Mechanistic utility was captured through Utility Descriptor Potentials, while interfacial penalty was captured through Rate and Stability Determining Limitations. Evidence completeness was assessed separately using structural, electrochemical, mechanistic, and anchoring characterization scores. Aggregate mechanistic utility (Sum_U) and mechanistic penalty (Sum_R) were then calculated deterministically and used to construct the median-referenced U–R space. Quadrant assignment depends only on these extracted descriptors evaluated under the fixed criteria; no post hoc rescoring, numerical tuning, or boundary adjustment was applied. Reported activity values were therefore used for performance comparison, but not for defining the U–R quadrant boundaries. The analysis was carried out in a fixed sequence in which descriptor values and evidence-completeness scores were assigned before U–R aggregation, whereas reported activity metrics were analysed only after the U–R landscape had been fixed. As an additional circularity sensitivity check, removing S3 mechanistic tendency labels from the interpretation did not change catalyst-level U–R quadrant assignments or the η_{10}–Sum_R divergence result (S13). The descriptor construction and aggregation are rule-based and deterministic, with no parameter fitting or optimization. The workflow was organized in seven section-wise layers. S1 defined catalyst identity, reaction class, support, and anchoring class. S2 recorded reported electrochemical metrics and medium without imputing missing values. S3 assigned OA, MLC, and PCET as mechanistic tendency weights, not proof of mechanism. S4 defined U1–U4 and R1–R4 from fixed utility and limitation rules. S5 added structural, electrochemical, mechanistic, and anchoring evidence scores. S6 added experimental-regime descriptors, and S7 generated the frozen U–R landscape using fixed medians. To make the scoring auditable, the offline CCR Viewer provides for each catalyst a literature-extraction card, a score-explanation card for U1–U4, R1–R4, SC, EC, MC, and AC, and an S7 verification block containing the numerical fields used for U–R placement. Complete extraction rules, descriptor definitions, and the full dataset are provided in the Supplementary Information and Supplementary Software; all assignments are contingent on reported literature data and reflect variations in reporting completeness.

3. Results

3.1 Distribution and scope of unified utility–penalty (U–R) space

Mechanistic utility (U) and mechanistic penalty (R) are defined as summed interfacial descriptor vectors derived from S4. Utility is computed as Sum_U = $\sum_{i=1}^{4} U_i$

where **U1**–**U4** quantify anchoring strength/film integrity, proton-relay and proton coupled electron transfer (PCET) environment, electronic coupling/redox communication, and operational durability, respectively. Similarly, penalty is computed as Sum_R =$\sum_{i=1}^{4} R_i$

where **R1**–**R4** quantify failure/deactivation risk, redox/electron transfer bottlenecks, structural instability, and mass-transport/accessibility limitations. All U_i and R_i values lie within [0,1] and are used without rescaling (S4). The obtained U–R space is divided into four quadrants using medians computed over the frozen dataset (n = 157; median(Sum_U) = 2.85; median(Sum_R) = 1.58; S7). Boundary cases are assigned to the higher side (≥ median). Quadrant definitions are

Q1: Sum_U ≥ median(Sum_U) and Sum_R ≥ median(Sum_R) (High U / High R)

Q2: Sum_U ≥ median(Sum_U) and Sum_R < median(Sum_R) (High U / Low R)

Q3: Sum_U < median(Sum_U) and Sum_R ≥ median(Sum_R) (Low U / High R)

Q4: Sum_U < median(Sum_U) and Sum_R < median(Sum_R) (Low U / Low R)

All subsequent references to utility, penalty behaviour, and exemplar locations are based strictly relative to these inequalities (S7).

When all 157 anchored molecular electrocatalysts are mapped into the U–R space, the distribution is non-uniform (Fig. 2a). Most systems fall across the two quadrants **Q2** and **Q3** (136/157), whereas **Q1** and especially **Q4** are sparsely populated (**Q1** = 13, **Q4** = 8; $\chi^2(3) = 84.554$, $p = 3.24 \times 10^{-18}$; S11). The test evaluates deviation from uniform quadrant occupancy across the four U–R categories. Sum_U and Sum_R are also strongly anticorrelated (Pearson r = −0.8959, $R^2 = 0.8027$, 95% CI [−0.9230, −0.8600], n = 157, $p = 1.71 \times 10^{-56}$) over the entire dataset. This yields a structured, diagonally organized distribution under the present descriptor construction. Because both U and R are constructed from the same literature records, they are not statistically independent at the dataset level. Our aim was not to establish independence between descriptor components, but to provide a structured representation of these contributions. Supporting perturbation results for individual descriptor components are provided in Section S6.

Quadrant occupancy varies significantly with anchoring category ($\chi^2(12) = 27.787$, p = 0.00594; Cramér's V = 0.243; n = 157), indicating an association between anchoring category and quadrant occupancy within the U–R space. Within the descriptor framework, anchoring is encoded explicitly through categorical assignment, whereas support contributions enter indirectly through descriptor components associated with electronic coupling and structural stability (U3, R2, R3). Differences in DesignEvidenceScore between quadrants (Kruskal–Wallis test: $H(3) = 85.915$, $p = 1.65 \times 10^{-18}$; $\varepsilon^2 = 0.542$; n = 157) indicate that evidence quality also varies across quadrants, with lower-penalty regions exhibiting higher average evidence completeness. This trend reflects higher median DesignEvidenceScore values in **Q2** relative to **Q1** and **Q3** within the compiled dataset. **Q2** contains systems with higher mechanistic utility and lower aggregate penalty. However, the co-modal population of **Q3** indicates that higher aggregate penalty frequently coincides with reduced mechanistic interpretability across reported anchored systems. High-penalty quadrants (**Q1** + **Q3**) contain 81/157 systems (51.6%). In these quadrants, elevated aggregate penalty and interfacial

View Article Online
DOI: 10.1039/D6TA02884F

limitations coincide with lower average evidence completeness relative to low-penalty regions (S4–S6).

Given the diagonally organized dataset, compositional patterns across quadrants are summarized using weighted composition rather than raw counts (Fig. 2b; S8). The **Q2** quadrant contains a relatively higher weighted proportion of PEC-OER systems and covalent or strongly interfacial anchoring modes, whereas the **Q3** quadrant contains a higher weighted proportion of HER systems with non-covalent anchoring. The relative contribution of mechanistic channels varies across the U–R landscape, with oxidative addition (OA) assigned a larger aggregate share in higher-utility quadrants and proton-coupled electron transfer (PCET) assigned a larger aggregate share in lower-utility quadrants. Together, these descriptive patterns indicate coordinated variation in reaction environment, anchoring chemistry, and mechanistic expression at the level of the anchored interfacial system.

The U–R landscape organizes catalysts by mechanistic utility and mechanistic penalty, while evidence quality is captured separately. Performance metrics in the reported literature summarize activity but do not directly reflect mechanistic utility, interfacial penalty, or evidence completeness and therefore do not capture this organization. As a result, systems occupying similar regions of U–R space can differ substantially in how well their proposed mechanisms are supported. Evidence completeness was evaluated separately through structural, electrochemical, mechanistic, and anchoring characterization scores, represented by DesignEvidenceScore, and summarized through the normalized Order Index (Fig. 2c).

When mapped onto the fixed U–R geometry, the Order Index shows wide variation in evidence strength even among systems occupying similar regions of U–R space. Although DesignEvidenceScore does not influence U–R construction, it nevertheless shows empirical correlation with both Sum_U and Sum_R (S11). This indicates that mechanistic position and evidence depth co-vary across the dataset, reflecting reporting differences rather than dependence between descriptor definitions. Systems with the highest evidence completeness represent only 15.9% cases (25/157) while low-tier systems form majority of the dataset (85/157, 54.1%). Low-tier systems are associated with limited experimental validation and, in many cases, higher aggregate penalties. Many of these systems report substantial catalytic activity and also claim a mechanistic pathway, but the available data do not support strong mechanistic confidence. The tier distribution therefore distinguishes evidence quality from catalytic performance while remaining conditional on the completeness of reported characterization.

3.2 Robustness and forward validation of the U–R landscape

Robustness of the U–R landscape was assessed by perturbing the raw order value (Order_raw) while keeping descriptor values, thresholds, and quadrant boundaries fixed. Multiplicative noise of ±5–15% was applied across 1000 Monte Carlo simulations at each level (n = 157). Tier assignments remained largely stable (Fig. 2d; S9). Even at ±15% perturbation, more than 90% of baseline high-tier systems remained unchanged, and no low-tier system shifted to high-tier. Changes occurred primarily among systems near the mid-tier boundary, most commonly through mid-to-low shifts. Quadrant positions were unaffected, as they depend only on the fixed utility and penalty medians.

The frozen U–R geometry enables direct forward mapping against newly reported literature under fixed descriptor rules.[14] Eight systems were projected into U–R space using the same medians (U = 2.85, R = 1.58) and extraction criteria (S10). No rescaling or adjustment was applied. Seven of these catalysts were published after construction of the original dataset, and one had been available but was not included in the initial review. Seven systems fall in quadrant Q3, while **Fe-41** occupies quadrant Q1 and lies close to the U-boundary; a decrease of 0.05 in Sum_U would shift it into **Q3**. Three π–π-anchored systems (**Fe-44**–**Fe-46**) and one interfacially anchored system (**Co-91**) lie within 0.07 of the utility boundary. A fourth π–π-anchored system (**Fe-47**) lies within 0.10 of the boundary. These small offsets indicate that several projected systems cluster near the utility boundary (Fig. 2d). In contrast, the non-covalently anchored systems in this forward set lie well below the utility median. This indicates that significant changes in Sum_U (≈0.25) are required to cross a quadrant boundary. These distances illustrate the sensitivity of quadrant assignment to the fixed U–R medians and also reveal that newly reported systems fall within the same regions defined by the original dataset. This analysis evaluates how additional systems map onto the existing U–R space without introducing predictive claims or modifying the descriptor scheme.

3.3 HER Regime

Under HER conditions, anchoring chemistry influences whether molecular pathways remain mechanistically interpretable after immobilization.[15] Across the full dataset, HER systems descriptively cluster within a limited region of U–R space characterized by high mechanistic utility and comparatively low mechanistic penalty (Fig. 3a). This observation is consistent with comparatively reduced interfacial constraints under HER conditions.[16] It highlights regimes in which matched proton delivery and electronic coupling allow anchoring to preserve chemically interpretable catalytic pathways (Fig. 3b). All three HER exemplars occupy the low-penalty, high-utility quadrant **Q2**, despite employing chemically distinct anchoring strategies. These exemplars show that multiple anchoring strategies can support mechanistic interpretation of HER under immobilized conditions when interfacial penalty is low and evidence is sufficiently complete. Effective HER anchoring is therefore associated with reduced penalty-inducing interfacial processes such that intrinsic molecular reactivity remains distinguishable after immobilization.

Fe-12 illustrates a conjugated, polymer-confined anchoring strategy in which a molecular [Fe–Fe] hydrogenase mimic is embedded within a pyrene-modified metallopolymer immobilized on carbon nanotube(s) (CNTs) (Fig. 3c).[17] Pyrene units provide π–π anchoring, while hydrophilic polymer segments maintain proton accessibility. Under neutral conditions, Fe-12 exhibits catalytic onset near −0.22 V vs RHE

View Article Online
DOI: 10.1039/D6TA00384E

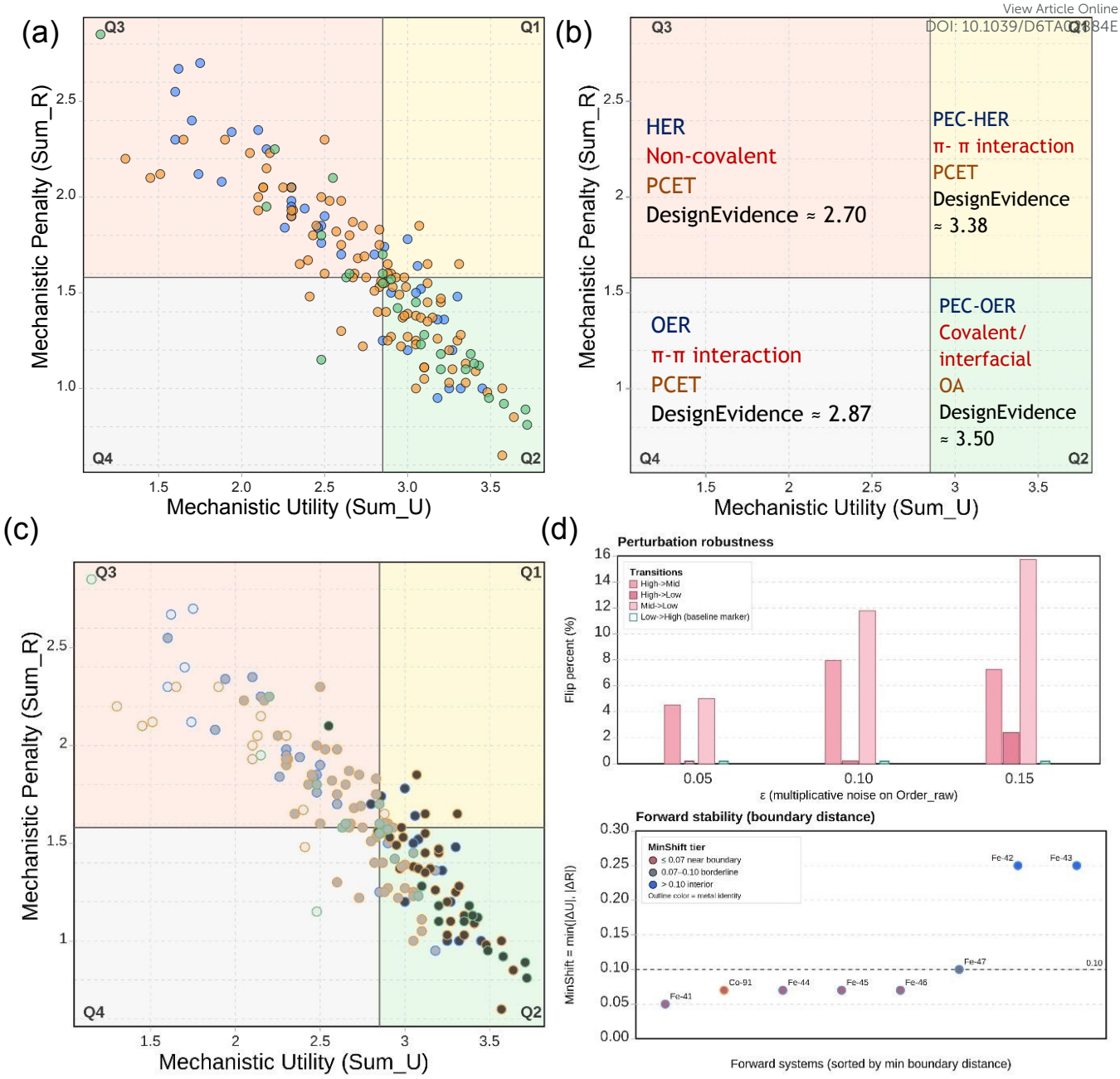

Fig. 2 U–R landscape and stability analysis. (a) Distribution of 157 anchored molecular electrocatalysts in U–R space. Fe, Co and Ni systems are coloured as blue, orange and green respectively. (b) Quadrant-level summary showing the most enriched reaction class and anchoring mode, dominant mechanistic channel, and mean DesignEvidenceScore values. (c) Evidence-tier encoding (Order Index) superimposed on the frozen U–R geometry. Order Index tiers are encoded by grayscale fill (pale → dark), where darker markers denote higher evidence completeness. (d) Sensitivity of Order Index tiers to multiplicative noise and placement of forward-projected systems relative to the fixed quadrant boundaries.

and reaches ~15 mA cm^{-2} at −0.6 V. Extended electrolysis (20 h) yields turnover number (TON) ≈ 3.1 × 10^5 and turnover frequency (TOF) ≈ 4.3 s^{-1}. **Fe-12** is associated with a PCET-dominated mechanistic weight and high evidence completeness, and despite gradual Fe-core degradation at long timescales, shows moderate aggregate penalty values.

Ni-18 reaches a similar low-penalty, high-utility quadrant **Q2** regime through an intrinsically extended coordination strategy. The catalyst forms an ultrathin (<1 nm) Ni–S–C covalent nanosheet deposited directly on glassy carbon (Fig. 3c).[18] The covalent Ni–S–C lattice provides structural and mechanical robustness as confirmed by AFM, TEM, GIXD, Raman, and XPS measurements. No detectable Ni(0) formation was observed in these experiments. Under acidic conditions, **Ni-18** displays ~12 h of stable operation with ~99% Faradaic efficiency while retaining activity over 500 cycles. A key feature is redox-switchable conductivity, which increases from ~3 × 10^{-6}–10^{-1} S cm^{-1} under HER conditions, indicating charge transport across the lattice. This behaviour is consistent with a low aggregate penalty and a dominant metal–ligand cooperativity channel.

Ni-1b represents the most structurally defined anchoring strategy among the exemplars. Ni bis(diphosphine) sites are covalently grafted onto carbon nanotubes via amide linkages and integrated into a CNT-based gas diffusion electrode (Fig.

View Article Online
DOI: 10.1039/D6TA02884E

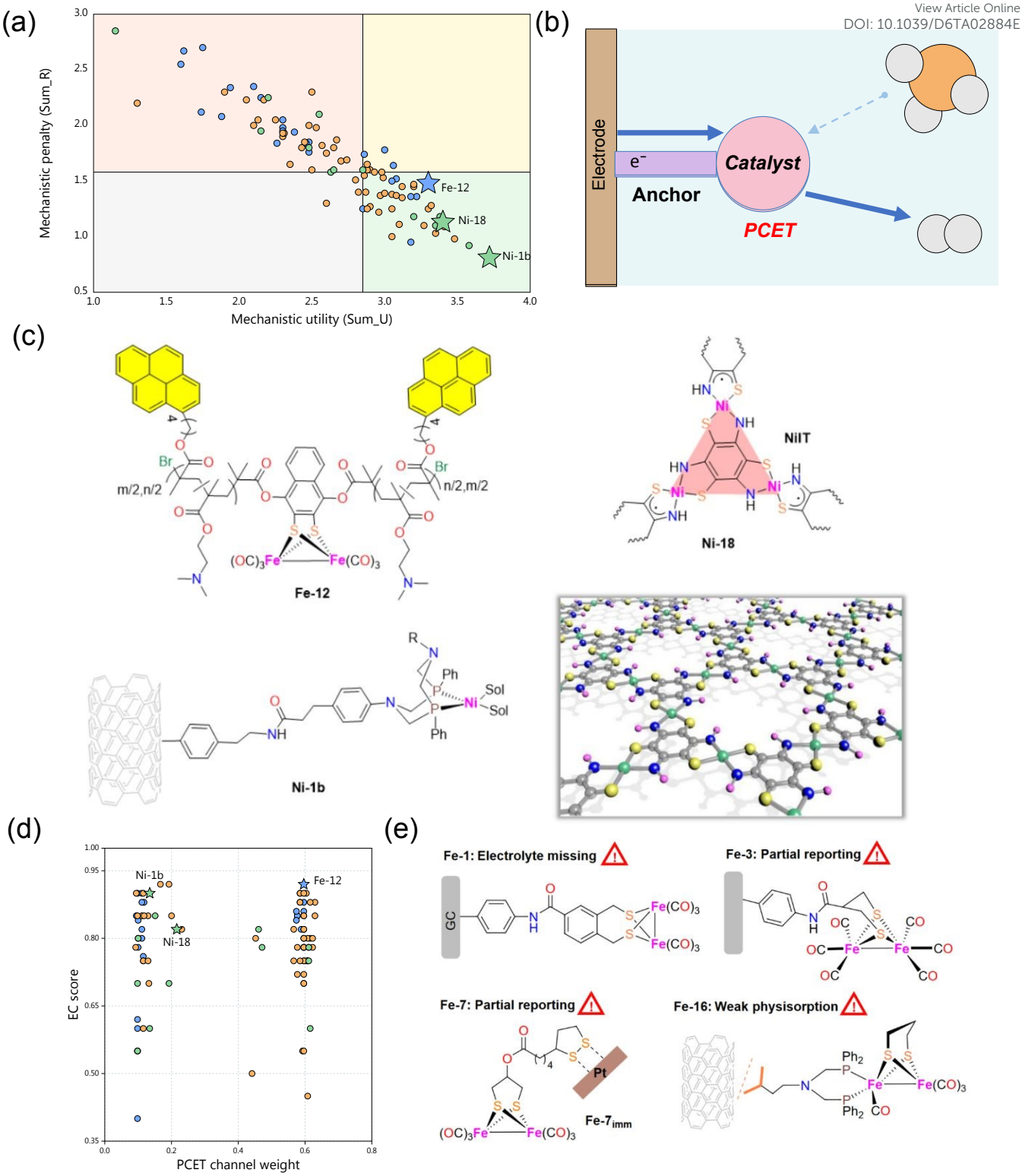

Fig. 3 Anchoring effects on HER systems in U–R space. (a) U–R distribution of HER systems with median quadrant boundaries. (b) PCET mechanism for anchored electrocatalysts. (c) HER exemplars showing different anchoring strategies. (d) ECOMP (evidence completeness) vs PCET channel weight for HER systems. (e) Anchored Fe catalysts with incomplete reporting, ambiguous anchoring, or weak physisorption that lead to higher penalty values.

3c).[19] The embedded proton-relay amines are proposed to regulate proton delivery and stabilize Ni–hydride intermediates, supporting assignment to a ligand-assisted HER pathway. In a strongly acidic medium, **Ni-1b** delivers ~10 mA cm^{-2} at overpotentials of ~60 mV at elevated temperature (85 °C) and remains stable for ~7 h at room temperature. Within U–R space, **Ni-1b** exhibits one of the lowest aggregate penalty values among HER systems (Sum_R = 0.81) and one of the highest Order Index values (≈0.99), supported by extensive

View Article Online
DOI: 10.1039/D6TA02884F

spectroscopic validation and consistent electrochemical reporting (Fig. 3d; S7).

Several iron-based systems report HER-related electrochemical responses but, unlike the exemplars, do not occupy regions of U–R space associated with stronger mechanistic support (Fig. 3e). In **Fe-1** and **Fe-3**, incomplete electrochemical reporting prevents reliable separation of intrinsic molecular behaviour from interface-dominated effects.[20,21] In **Fe-7**, ambiguous anchoring verification clouds whether observed currents arise from the molecular species or from altered interfacial states formed during operation.[22] For **Fe-16**, weak physisorption permits apparent PCET-like behaviour at short timescales. However, this weak anchoring leads to elevated aggregate penalties and mechanistic drift under operation.[23] Within the HER regime, the U–R landscape shows that mechanistic interpretability varies with the balance between interfacial penalty, mechanistic utility, and the completeness of supporting evidence. Systems with lower aggregate penalty and higher evidence completeness are more consistently associated with interpretable molecular pathways, whereas elevated penalty or limited evidence reduces mechanistic confidence even when catalytic activity is observed.

3.4 OER Regime

Under oxygen evolution conditions, anchored molecular electrocatalysts experience comparatively higher mechanistic penalties within the analysed dataset.[24] Unlike HER, where proton-coupled electron transfer pathways can in some cases be preserved after immobilization, OER requires sustained access to high-valent metal oxidation states, multi-electron transfer, and O–O bond formation under strongly oxidative bias, typically at significant overpotential (Fig. 4a).[25] Under OER conditions, anchoring influences which molecular pathways remain accessible at the interface and whether high-valent catalytic cycles can be sustained without incurring substantial mechanistic penalty.[26] This behaviour is reflected in the OER-specific distribution within the U–R space (Fig. 4b). In this dataset, OER systems partition primarily between quadrants **Q2** and **Q3**, with no systems occupying the **Q1** quadrant. Among OER systems with stronger mechanistic support, pathways requiring access to M–OH, M=O, and M–OOH intermediates are observed, consistent with the requirements of OER chemistry. At the same time, the strong metal–oxygen bonding and high oxidation states that enable OER also contribute to increased penalty after anchoring.[27] OER exemplars are selected according to how anchoring strategies, interfacial composites, or redox-active ligands redistribute oxidative burden within the catalytic system.

Fe-40 exemplifies an OER case where anchoring and axial ligation support access to a high-valent manifold. The imidazole-tethered iron porphyrin immobilized on CNTs achieves high mechanistic utility with finite but non-negligible penalty. DFT analysis indicates that O–O bond formation proceeds via nucleophilic OH^- attack on a formal $[Fe^{V}=O]^{+}$ species (more accurately described as $\bullet L^{+}–Fe^{III}–O\bullet$), consistent with ligand redox non-innocence (Fig. 4c).[28] Post operando characterization suggests retention of molecular identity and O_2 FE >98%. The penalty profile for **Fe-40** is dominated by structural and electronic burdens (R3 and R2; Fig. 4e; S4 and S5), consistent with repeated access to high-valent Fe–oxo states under oxidative bias. In this case, anchoring enables access to these intermediates but does not eliminate the associated penalty.

For **Co-14**, anchoring reduces interfacial failure pathways, yet an overall penalty remains.[29] Although it exhibits high mechanistic utility and retains molecular features after anchoring, its behaviour is governed by polymer–inorganic interfacial cooperativity (Fig. 4d). The polymeric cobalt phthalocyanine overlayer on Co_3O_4/CoP nanosheets lowers charge-transfer resistance and yields a low Tafel slope and sustained OER operation (>20 h). This suggests that mechanistic utility arises from distributed redox accessibility and buffered interfacial charge delivery rather than stabilization of a high-valent Co–oxo intermediate. The low aggregate penalty reflects the absence of dominant structural reorganization, environmental sensitivity, or transport limitation. **Co-14** therefore represents an interfacial OER system where composite anchoring reduces dominant failure modes without eliminating penalty entirely.

Co-60a represents a case where covalent anchoring supports retention of a molecular OER cycle under oxidative conditions.[30] A short, conjugated linker anchors cobalt corrole to CNTs, enabling efficient charge transfer and access to formal Co(V) intermediates with reduced susceptibility to common oxidative degradation pathways. Electrochemical kinetics and post operando characterization are consistent with an OA-dominated, molecular OER pathway with low aggregate penalty, placing **Co-60a** in a high-utility, low-penalty quadrant **Q2**. Approximately 40% of cobalt OER systems populate quadrant **Q3**. Systems such as **Co-54**,[31] **Co-60b**,[30] **Co-73**,[32] **Co-74**,[33] and **Co-81**[34] occupy **Q3–Q4** regions of U–R space, where mechanistic interpretation is less strongly supported under the reported conditions. Under sustained oxidative bias, anchoring may not sufficiently limit high-valent cycling, allowing interfacial reconstruction or irreversible transformation to contribute to observed OER currents. Without explicit consideration of interfacial penalty, such systems could be misinterpreted as molecular OER catalysts based solely on current–potential metrics. Within the OER regime, mechanistic interpretability varies with the balance between interfacial penalty, mechanistic utility, and the completeness of supporting evidence. Stabilizing high-valent intermediates and preserving molecular identity under oxidative bias are therefore important for maintaining interpretable molecular behaviour under these conditions.

3.5 PEC Regime

Under PEC operation, the driving force is supplied by photogenerated charge carriers rather than an applied bias.[35,36] This does not alter the molecular coordination chemistry of the catalyst but changes how the system is driven.[37,38] In PEC architectures, light generates electron–hole pairs within a semiconductor or dye–sensitized assembly, and only one carrier

View Article Online
DOI: 10.1039/D6TA02884E

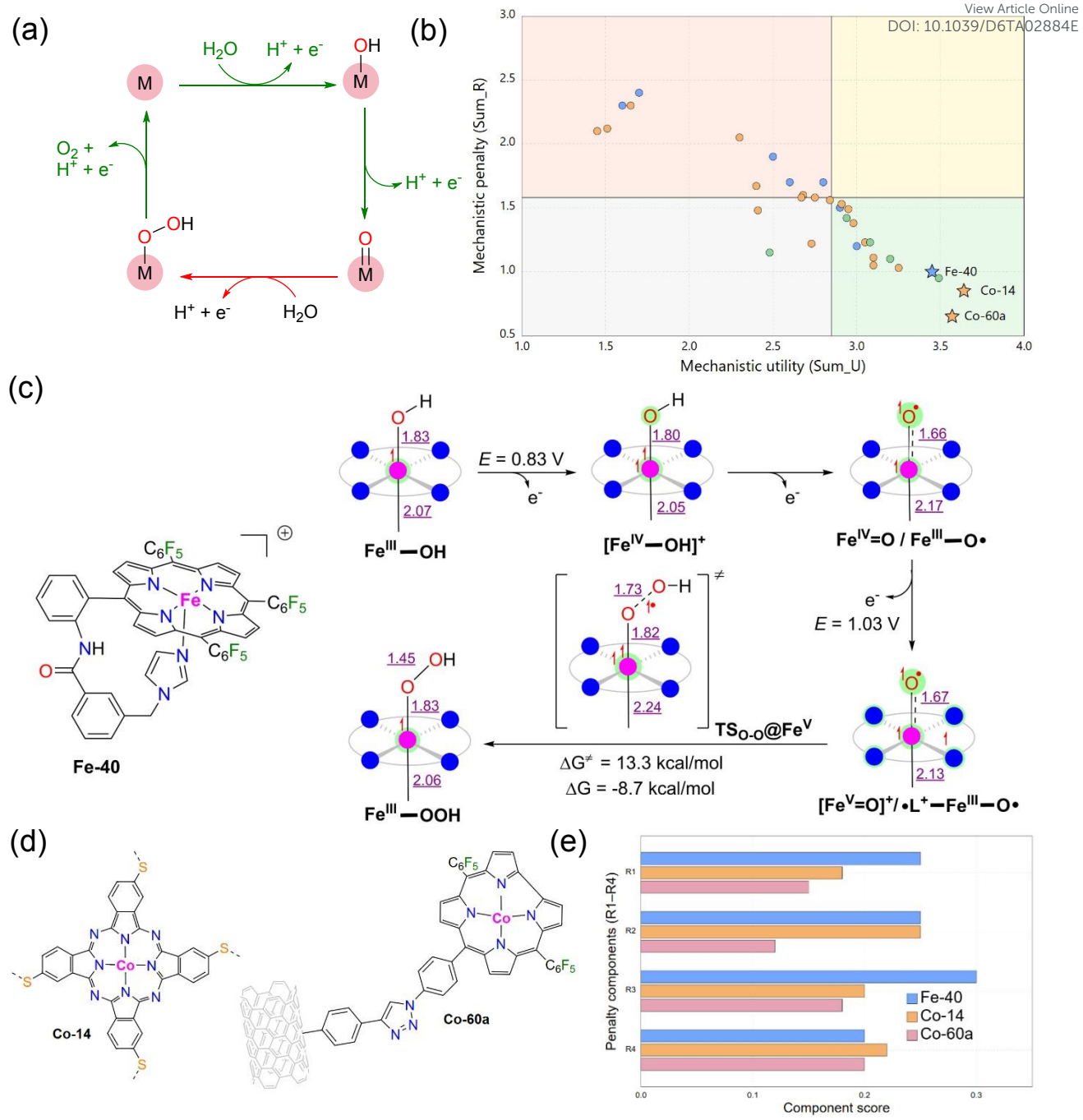

Fig. 4 OER systems in U–R space. (a) OER catalytic cycle showing O–O bond formation. (b) U–R distribution of OER systems with median quadrant boundaries. (c) DFT-calculated reaction pathway for **Fe-40**. (d) Molecular structures of representative OER systems (**Co-14** and **Co-60a**), illustrating differences in coordination environment and anchoring strategy. (e) Penalty components (R1–R4) for selected OER exemplars.

type reaches the anchored catalyst (Fig. 5a).[39] Charge generation is therefore spatially separated from catalysis.[40] As a result, conventional electrochemical limitations such as uncompensated resistance or external mass transport are replaced by photovoltage limits, recombination losses, and charge-transfer mismatches.[41]

These effects are most evident in PEC-HER systems, which tend to cluster at relatively high utility with moderate penalties (Fig. 5f). PCET frequently appears as a dominant utility channel, reflecting coupled proton delivery and electron injection at the anchored site under cathodic illumination.[42] For **Ni-10**, photogenerated electrons are transferred from p-Si through a mesoporous TiO_2 layer to the NiP motif, which retains its PCET character under PEC-HER conditions (Fig. 5b).[43] The mesoporous interlayer improves charge delivery and reduces instability, placing **Ni-10** in quadrant **Q2**.[44] **Co-44** represents a different structural solution to the same problem. Immobilization on ALD-TiO_2 establishes strong interfacial coupling, preserves molecular integrity, and enables sustained charge transfer under illumination (Fig. 5c).[45] The cobalt centre operates through a redox–hydride pathway consistent with established cobaloxime HER chemistry.[46] As a result, **Co-44** also

View Article Online
DOI: 10.1039/D5TA02884E

falls in quadrant **Q2**, despite differences in metal identity and ligand properties relative to **Ni-10**.

For **Co-52**, the dye HOMO and LUMO levels align with the Co(III/II) and Co(II/I) couples, allowing photogenerated electrons to reach catalytically relevant Co(I) states under illumination (Fig. 5d).[47] The resulting pathway is consistent with OA-weighted molecular HER behaviour within the U–R analysis. Still, the overall penalty remains high and is dominated by interfacial losses and recombination rather than catalyst instability. The low Faradaic efficiency and spectroscopic evidence of competing NiO support reduction (Ni^0 formation) indicate substantial substrate and charge-recombination constraints that illumination alone does not overcome. **Co-52** therefore falls in quadrant **Q1**. Access to the molecular pathway is achieved, but materials-level limitations reduce mechanistic confidence under the reported conditions.

In contrast, PEC-OER requires sustained access to high-valent metal intermediates, multi-electron transfer reactions, and O–O bond formation under strongly oxidative interfacial conditions.[48] These requirements are associated with increased interfacial penalty, and only systems that achieve both high mechanistic utility and controlled penalty are more consistently associated with interpretable behaviour under PEC-OER conditions. The PEC-OER subset is therefore small and occupies a region of high utility with finite, non-zero penalty. Illumination can enable access to molecular OER pathways but does not remove the intrinsic oxidative demands. **Fe-39** represents a well-characterized PEC-OER case, where covalent phosphonate anchoring to WO_3 enables access to high-valent Fe–oxo intermediates, yielding ~60% photocurrent enhancement relative to bare WO_3 and an O_2 Faradaic efficiency of 79 ± 9% (as reported) (Fig. 5e).[49] Mechanistic utility is PCET-dominated, while penalty remains finite, reflecting intrinsic oxidative and reorganizational demands rather than anchoring failure.

When anchoring or interfacial coupling is weaker, illumination does not necessarily improve mechanistic interpretability. Instead, operation can promote interfacial reconstruction or partial loss of molecular identity, leading to elevated penalty despite photogenerated charge carriers. This behaviour is illustrated by PEC-HER contrast cases such as **Co-32**[50] and **Fe-29**,[51] which exhibit weak physisorption or insufficient interfacial coupling and consequently occupy penalty-dominated regions of U–R space (Fig. 5g). Interestingly, **Co-79** serves as a complementary example where reported evidence supports molecular-identity retention under PEC–OER conditions.[52] Integration of CoTCPP on $BiVO_4$ reduces charge-transfer resistance from ~31 kΩ to ~7 kΩ and delivers ~2.1 mA cm^{-2} at 1.23 V vs RHE while maintaining ~80% O_2 FE. The system remains in a high-utility, finite-penalty **Q2** quadrant, indicating that its limitations arise from the challenging OER conditions and related interfacial processes rather than anchoring instability alone.

Illumination affects charge transport but does not directly alter the molecular coordination chemistry within the present descriptor definition.[53] The same U–R space applies, but its population shifts depending on how charges are generated and delivered to the catalytic site. PEC-HER systems often show lower effective penalty when anchoring and energy alignment are favourable, whereas PEC-OER remains associated with higher penalty due to oxidative conditions and interfacial demands. Separating mechanistic utility from penalty distinguishes PEC systems with stronger mechanistic support from those limited by interfacial and oxidative effects.

3.6 Performance–Interpretability Divergence

Performance metrics such as overpotential at 10 mA cm^{-2} (η_{10}) are widely used to benchmark anchored molecular electrocatalysts. η_{10} is reported for 59 of 157 catalysts and shows a moderate correlation with aggregate mechanistic penalty (Pearson r = 0.5436, p = 8.62 × 10^{-6}; Spearman ρ = 0.5031, p = 4.89 × 10^{-5}, S11). These values indicate that activity and penalty are partially coupled but not diagnostically equivalent descriptors. Systems with comparable η_{10} values may therefore occupy distinct regions of U–R space once anchoring-associated penalties are made explicit (Fig. 6a).[54]

To evaluate this divergence without relying on pairwise comparisons, η_{10} values were subdivided into quintiles within the reporting subset. The best-activity quintile (lowest 20% η_{10} values) does not map exclusively onto low-penalty, high-evidence systems. Across the η_{10}-reported systems, 40.68% occupy high-penalty quadrants (**Q1**+**Q3**), and 55.93% are in the lowest evidence tier. Even within the best activity quintile, 33.33% of systems reside in either high-penalty quadrants or the lowest evidence tier (Fig. 6b). Although these systems deliver significant current under the reported conditions, their position in the U–R space indicates that mechanistic attribution is less strongly supported within the reported interfacial context.

This divergence is further reflected in the distribution of combined penalty and evidence deficits. Within the 59 catalysts reporting η_{10}, 35.59% fall in the high-penalty and lowest-evidence category. An additional 11.86% fall in **Q2** but are supported by the lowest evidence tier. Low penalty by itself is therefore not sufficient to support a clear mechanistic assignment when validation is limited. When the data are stratified by the bases reported (pH > 10; n = 21; S6), the correlation between η_{10} and penalty becomes negligible (r ≈ 0.022). This suggests that the relationship between activity and penalty depends on reporting context. These results show that high activity does not consistently align with stronger mechanistic support for anchored systems. Catalysts with similar η_{10} values can differ markedly in interfacial penalty and in the strength of supporting evidence. The U–R space enables distinction between systems where mechanistic interpretation is more strongly supported and those where it is associated with higher penalty or limited validation.

Boundary cases further show why activity, U–R position, and evidence completeness need to be considered separately. Some systems fall in the high-utility/low-penalty **Q2** region but remain in the low evidence tier. **Co-10** reports a low η_{10} value of 0.081 V and is located in **Q2**, but remains in the low evidence tier.[55] Such cases are better viewed as promising but less validated. Conversely, some high-evidence systems can occupy high-penalty regions. For example, **Fe-18** is a high-tier HER

View Article Online
DOI: 10.1039/D6TA02884E

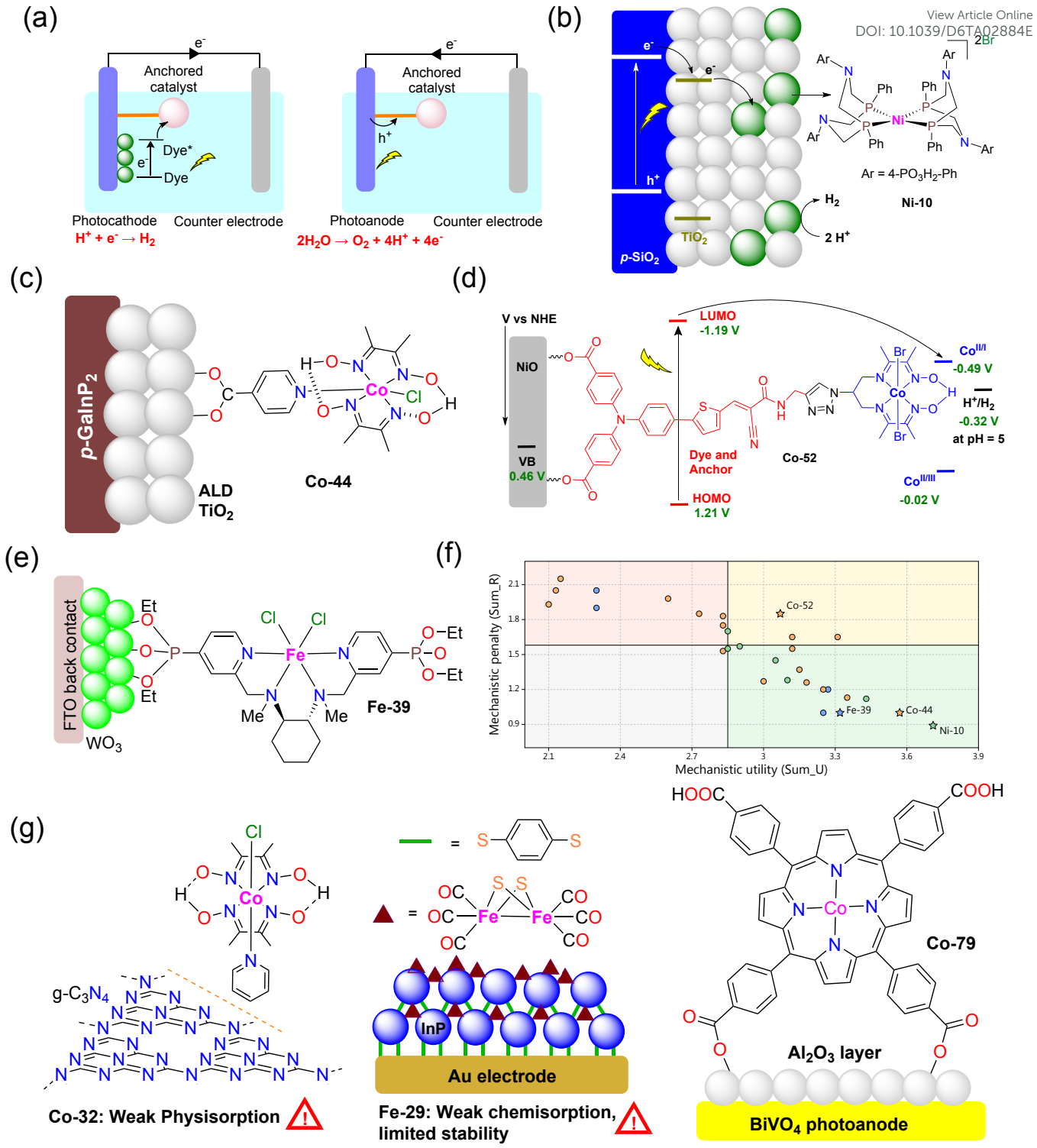

Fig. 5 PEC–HER and PEC–OER systems in U–R space. (a) Schematic representation of PEC-HER and PEC-OER. (b) PEC–HER catalyst **Ni-10**, showing electron injection from p-Si to the molecular catalyst via TiO_2. (c) **Co-44** immobilized on ALD-TiO_2 by covalent attachment. (d) Energy-levels for HOMO and LUMO in **Co-52**. (e) PEC–OER exemplar **Fe-39** anchored on WO_3/FTO (fluorine-doped tin oxide). (f) U–R distribution of PEC systems with median quadrant boundaries. (g) **Co-32** and **Fe-29** are PEC–HER systems with higher mechanistic penalty. In contrast, **Co-79** is a PEC–OER system limited by the inherent demands of PEC-OER.

system located in **Q1**, but has a high η_{10} value of 0.930 V with elevated aggregate penalty.[56] These cases show that evidence completeness helps diagnose the interfacial state, but does not ensure low penalty or unambiguous molecular operation.

3.7 Design Constraints Revealed by the U–R Landscape

As discussed, the U–R space fixes each system's position using predefined criteria and fixed median boundaries, while evidence completeness is evaluated independently through the

View Article Online
DOI: 10.1039/D6TA02884E

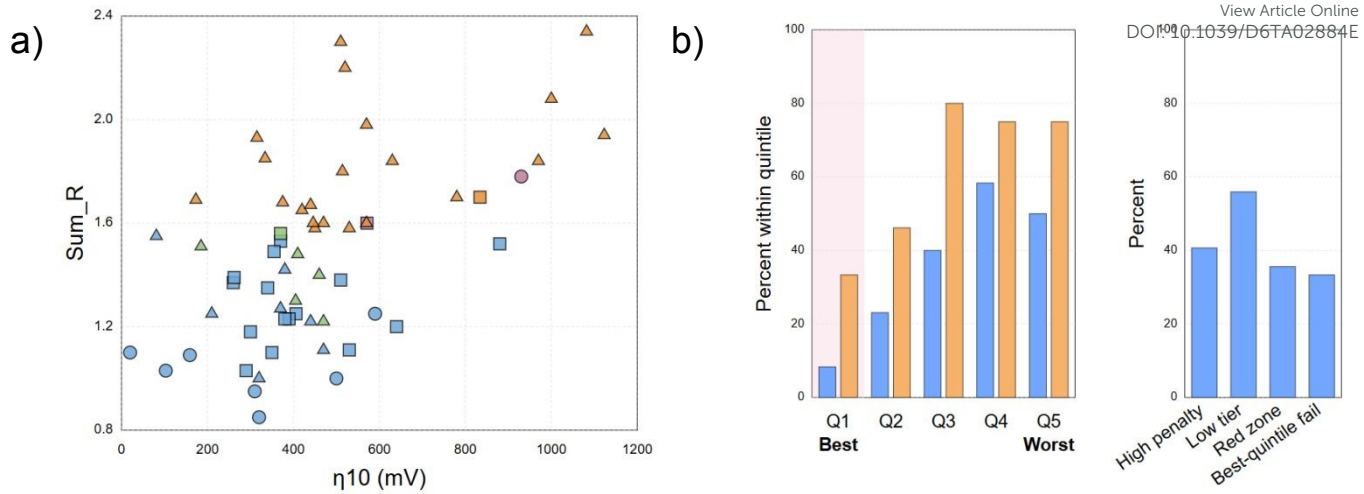

Fig. 6 Measured activity is not a unique indicator of mechanistic reliability in anchored systems. (a) Overpotential at 10 mA cm^{-2} (η_{10}, converted to mV) versus aggregate mechanistic penalty (Sum_R) for the η_{10}-reporting subset (n = 59 of 157). Association between η_{10} and Sum_R was assessed using two-tailed Pearson (r = 0.5436, p = 8.62×10^{-6}) and Spearman (ρ = 0.5031, p = 4.89×10^{-5}) correlations. Points are coloured by quadrant (**Q1–Q4** defined by frozen medians Sum_U = 2.85 and Sum_R = 1.58; blue **Q1**, green **Q2**, orange **Q3**, mauve **Q4**) and shaped by evidence tier (circle = High, square = Mid, triangle = Low). (b) Quintile-based activity band risk within the η_{10}-reporting subset. Within the η_{10} subset, 40.68% occupy high-penalty quadrants (**Q1**+**Q3**), and 55.93% fall in the lowest evidence tier.

Order Index. This separation allows mechanistic interpretability to be assessed without conflating activity metrics with evidential support, although these quantities may vary together across the dataset. Across reaction classes, anchoring influences how mechanistic interpretation can be supported under interfacial conditions. The framework can therefore be used as a simple checklist to report the activity, assess anchoring, compare with proper controls, check the catalyst after electrolysis, and consider interfacial limitations separately (Fig. 7).

In HER systems, increasing PCET character does not by itself strengthen mechanistic support when anchoring-related penalty remains high. Systems that exceed the median penalty are more often associated with reduced mechanistic support unless attachment stability and interfacial integrity are well established. In OER, this behaviour is more pronounced. High molecular utility, such as favourable redox matching or coordination environment, does not prevent migration into higher-penalty regions when the anchored structure is unstable under oxidative bias. In such cases, chemical plausibility of a pathway does not compensate for limited interfacial stabilization.

Photoelectrochemical operation modifies charge delivery and recombination dynamics but does not remove interfacial or oxidative limitations. Illumination may change current profiles, yet systems remain governed by the same underlying stability and interfacial factors. Photodriven conditions therefore do not necessarily reduce interfacial penalty. These observations indicate that anchoring influences the reliability with which mechanisms can be interpreted under immobilized conditions. Molecular design, interfacial stability, and depth of validation operate together, and improvement in one dimension does not automatically resolve limitations in the others.

The anchoring mode also affects how much confidence can be placed on the activity data. Covalent attachment can reduce simple desorption, but it does not remove all problems. The linker may degrade, grafting may be incomplete, or the electron-transfer pathway may change after attachment. Any of these can affect the measured response. Coordination or phosphonate anchoring on oxides and semiconductors often supports PEC systems, but pH-dependent desorption, ligand exchange, or surface reconstruction must be considered. Electrostatic adsorption is more vulnerable to leaching, ion exchange, and film redistribution during electrolysis. π–π interactions between aromatic molecular units and graphitic carbon supports such as CNTs can improve contact with the electrode. But aggregation, multilayer formation, and support-derived current remain possible. Therefore, no anchoring mode should be treated as automatically reliable. The relevant checks should follow the likely failure mode such as post operando spectroscopy for covalent systems, binding and retention tests for coordination or phosphonate systems, rinse transfer and ICP leaching tests for electrostatic films, and loading dependence and support-only controls for π–π-stacked systems. These checks reduce anchoring-specific ambiguity but do not by themselves prove molecular operation.

Beyond HER, OER, and PEC reactions, the U–R framework could also be extended in future to electrocatalytic nitrogen oxide conversion and related reactions.[57,58] However, these reactions are associated with additional challenges such as competing intermediates, HER competition, and catalyst or support changes during operation.[59,60] Additional descriptors for identifying the active nitrogen-containing species, product selectivity, and post operando structural stability might be necessary in such analysis.

4. Conclusion

Our analysis indicates that reported differences in anchored molecular electrocatalysis often reflect differences in mechanistic validation rather than necessarily incompatible

View Article Online
DOI: 10.1039/D6TA03884E

chemistry. Low overpotentials or high current densities can arise from transport effects, catalyst loading, or interfacial restructuring, and do not by themselves establish a defined molecular pathway. When anchoring integrity and molecular persistence under bias are not directly verified, mechanistic attribution remains uncertain. Across the systems analysed, identical molecular scaffolds are associated with different levels of mechanistic interpretability depending on interfacial context. Stable attachment, limited structural evolution, and internally consistent charge and mass transport are commonly observed features of systems with stronger mechanistic support. Under oxidative and photoelectrochemical conditions, these requirements become more pronounced, reflecting the increased structural and redox demands of operation.

The U–R analysis was used to compare reported activity, penalty from the anchoring/interface, and the amount of supporting evidence as three separate issues. Treating these points separately helps identify cases where the mechanistic assignment is reasonably supported, and cases where good activity is reported but the supporting validation is still limited. These results suggest that anchored molecular electrocatalysts should not be judged from activity values alone. Future studies also need clearer evidence for the structure, interface, and stability of the catalyst during operation.

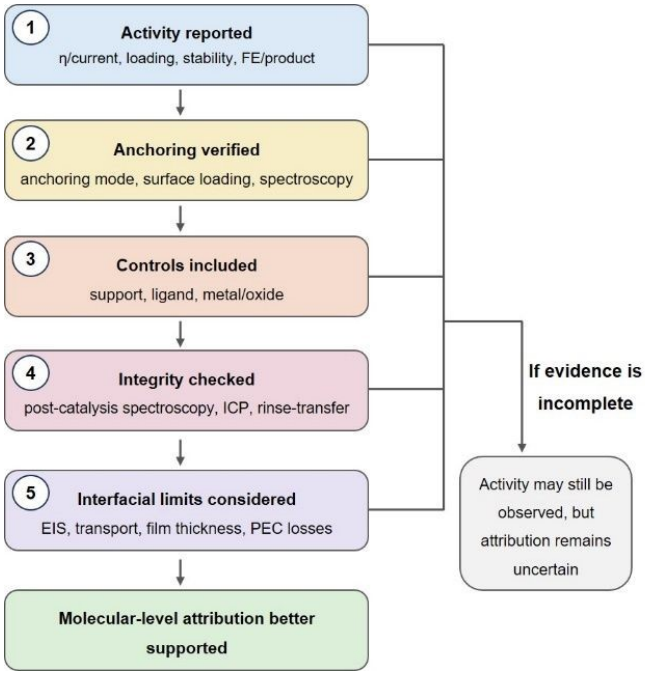

Fig. 7 Stepwise check for molecular-level attribution. The workflow separates reported activity from molecular-level assignment by assessing anchoring, controls, post-catalysis integrity, and interfacial or PEC-related limitations.

Author contributions

A.S.–conceptualization, methodology, formal analysis, validation, visualization, project administration, supervision, writing–original draft, writing–review & editing. S.G.–conceptualization, methodology, supervision, validation, writing–review & editing. A.P.N.–investigation, data curation, formal analysis. A.R.–investigation, data curation, formal analysis. D.D.–investigation, data curation, writing–review & editing. P.B. – investigation, data curation, writing–review & editing. T.G.–validation, writing–review & editing. B.S.–validation, writing–review & editing. K.S.–validation, writing–review & editing. All authors reviewed and approved the final manuscript.

Conflicts of interest

There are no conflicts to declare.

Data availability

All data supporting this study are available in the article and its Electronic Supplementary Information (ESI), together with the accompanying Supplementary Dataset. The dataset contains the catalyst-level extracted literature information, descriptor values, evidence-completeness scores, U–R placement, robustness checks, forward-validation data, statistical outputs, figure source data, extraction rules, and verification scripts. We have also provided the offline file CCR_Viewer.html. This file allows each catalyst entry to be checked individually, including the extracted literature information, scoring details, and quadrant placement. All data were compiled from publicly available literature sources cited in the manuscript; no new experimental or crystallographic data were generated. See DOI:xxxxxxx

Acknowledgements

A.S. acknowledges ANRF and SERB start–up research grant (SRG/2023/000037) for funding. S.G. thanks VIT for providing a Seed Grant (SG20230076). A.S. and S.G. thank VIT for laboratory and instrumental facilities.

Notes and references

1 D. P. Hickey and S. D. Minteer, *Joule*, 2019, **3**, 1819–1821.
2 J. Wang, S. Dou and X. Wang, *Sci. Adv.*, 2021, **7**, eabf3989.
3 L. Sévery, J. Szczerbiński and M. Taskin, *Nat. Chem.*, 2021, **13**, 523–529.
4 H. Bemana, M. McKee and N. Kornienko, *Chem. Sci.*, 2023, **14**, 13696–13712.
5 T. E. Rosser and E. Reisner, *ACS Catal.*, 2017, **7**, 3131–3141.
6 R. M. Bullock, A. K. Das and A. M. Appel, *Chem. Eur. J.*, 2017, **23**, 7626–7641.
7 C. Costentin and J.-M. Savéant, *ChemElectroChem*, 2014, **1**, 1226–1236.
8 J. Fernández-Vidal and M. T. M. Koper, *ACS Catal.*, 2026, **16**, 2925–2934.
9 J.-M. Savéant, *Chem. Rev.*, 2008, **108**, 2348–2378.
10 H. Dau, C. Limberg, T. Reier, M. Risch, S. Roggan and P. Strasser, *ChemCatChem*, 2010, **2**, 724–761.
11 T. Singh, S. Ghosh and A. Sarbajna, *Coord. Chem. Rev.*, 2026, **546**, 217071.
12 A. Prajapati, C. Hahn, I. M. Weidinger, Y. Shi, Y. Lee, A. N. Alexandrova, D. Thompson, S. R. Bare, S. Chen, S. Yan and N. Kornienko, *Nat. Commun.*, 2025, **16**, 2593.

13 R. Said, M. K. Abosaoda, N. A. Ibrahim, M. M. Rekha, S. Ray, K. Chennakesavulu, R. Sharma, A. Pramanik and G. Ramaiah, *Electrochem. Commun.*, 2026, **182**, 108094.
14 C. M. Bishop, *Pattern Recognition and Machine Learning*, Springer, New York, 2006.
15 A. I. Osman, A. Ayadi, P. Krivoshapkin, B. Tanhai, M. Farghali, P.-S. Yap and A. Abdelhaleem, *Coord. Chem. Rev.*, 2024, **514**, 215900.
16 J. Zhu, L. Hu, P. Zhao, L. Y. S. Lee and K.-Y. Wong, *Chem. Rev.*, 2020, **120**, 851–918.
17 A. Zamader, B. Reuillard, P. Marcasuzaa, A. Bousquet, L. Billon, J. J. Espí Gallart, G. Berggren and V. Artero, *ACS Catal.*, 2023, **13**, 1246–1256.
18 X. Sun, K.-H. Wu, R. Sakamoto, T. Kusamoto, H. Maeda, X. Ni, W. Jiang, F. Liu, S. Sasaki, H. Masunaga and H. Nishihara, *Chem. Sci.*, 2017, **8**, 8078–8085.
19 T. N. Huan, R. T. Jane, A. Benayad, L. Guetaz, P. D. Tran and V. Artero, *Energy Environ. Sci.*, 2016, **9**, 940–947.
20 V. Vijaikanth, J.-F. Capon, F. Gloaguen, P. Schollhammer and J. Talarmin, *Electrochem. Commun.*, 2005, **7**, 427–430.
21 C. M. Thomas, O. Rüdiger, T. Liu, C. E. Carson, M. B. Hall and M. Y. Darensbourg, *Organometallics*, 2007, **26**, 3976–3984.
22 S. Benndorf, S. Groni, L. M. Stafast, H. Görls, C. Fave, B. Schöllhorn and W. Weigand, *Eur. J. Inorg. Chem.*, 2023, **2023**, e202200684.
23 S.-J. Wang, X. Bai, X. Su, T.-F. Wang, Y.-B. He and P.-H. Zhao, *Electrochim. Acta*, 2025, **524**, 145986.
24 E. Fabbri and T. J. Schmidt, *ACS Catal.*, 2018, **8**, 9765–9774.
25 X.-P. Zhang, A. Chandra, Y.-M. Lee, R. Cao, K. Ray and W. Nam, *Chem. Soc. Rev.*, 2021, **50**, 4804–4811.
26 T. R. Cook, D. K. Dogutan, S. Y. Reece, Y. Surendranath, T. S. Teets and D. G. Nocera, *Chem. Rev.*, 2010, **110**, 6474–6502.
27 M. W. Kanan and D. G. Nocera, *Science*, 2008, **321**, 1072–1075.
28 L. Xie, X.-P. Zhang, B. Zhao, P. Li, J. Qi, X. Guo, B. Wang, H. Lei, W. Zhang, U.-P. Apfel and R. Cao, *Angew. Chem. Int. Ed.*, 2021, **60**, 7576–7581.
29 Y. Kim, D. Kim, J. Lee, L. Y. S. Lee and D. K. P. Ng, *Adv. Funct. Mater.*, 2021, **31**, 2103290.
30 X. Li, H. Lei, J. Liu, X. Zhao, S. Ding, Z. Zhang, X. Tao, W. Zhang, W. Wang, X. Zheng and R. Cao, *Angew. Chem. Int. Ed.*, 2018, **57**, 15070–15075.
31 H. Lei, C. Liu, Z. Wang, Z. Zhang, M. Zhang, X. Chang, W. Zhang and R. Cao, *ACS Catal.*, 2016, **6**, 6429–6437.
32 I. K. Attatsi, W. Zhu and X. Liang, *New J. Chem.*, 2020, **44**, 4340–4345.
33 H. Qin, Y. Wang, B. Wang, X. Duan, H. Lei, X. Zhang, H. Zheng, W. Zhang and R. Cao, *J. Energy Chem.*, 2021, **53**, 77–81.
34 N. Morlanés, K. S. Joya, K. Takanabe and V. Rodionov, *Eur. J. Inorg. Chem.*, 2015, 49–52.
35 B. Zhang and L. Sun, *Chem. Soc. Rev.*, 2019, **48**, 2216–2264.
36 36 Y. Zhu, D. Wang, Q. Huang, J. Du, L. Sun, F. Li and T. J. Meyer, *Nat. Commun.*, 2020, **11**, 4610.
37 Z. Xi and M. Liu, *npj Mater. Sustain.*, 2025, **3**, 18.
38 J. Willkomm, K. L. Orchard, A. Reynal, E. Pastor, J. R. Durrant and E. Reisner, *Chem. Soc. Rev.*, 2016, **45**, 9–23.
39 T. Hisatomi, J. Kubota and K. Domen, *Chem. Soc. Rev.*, 2014, **43**, 7520–7535.
40 L. Fei, L. Lei, T. J. Meyer and D. Wang, *Acc. Mater. Res.*, 2024, **5**, 124–135.
41 Z. G. Schichtl, O. Q. Carvalho, J. Tan, S. S. Saund, D. Ghoshal, L. M. Wilder, M. K. Gish, A. C. Nielander, M. B. Stevens and A. L. Greenaway, *Chem. Rev.*, 2025, **125**, 4768–4839.
42 D. G. Nocera, *J. Am. Chem. Soc.*, 2022, **144**, 1069–1081.
43 J. J. Leung, J. Warnan, D. H. Nam, J. Z. Zhang, J. Willkomm and E. Reisner, *Chem. Sci.*, 2017, **8**, 5172–5180.
44 L. Chen and Q. Xu, *Matter*, 2019, **1**, 57–89.
45 J. Gu, Y. Yan, J. L. Young, K. X. Steirer, N. R. Neale and J. A. Turner, *Nat. Mater.*, 2016, **15**, 456–460.
46 J. L. Dempsey, B. S. Brunschwig, J. R. Winkler and H. B. Gray, *Acc. Chem. Res.*, 2009, **42**, 1995–2004.
47 N. Kaeffer, J. Massin, C. Lebrun, O. Renault, M. Chavarot-Kerlidou and V. Artero, *J. Am. Chem. Soc.*, 2016, **138**, 12308–12311.
48 F. Amano, in *Solar-to-Chemical Conversion: Photocatalytic and Photoelectrochemical Processes*, ed. H. Sun, Wiley-VCH, 2021, pp. 163–184.
49 B. M. Klepser and B. M. Bartlett, *J. Am. Chem. Soc.*, 2014, **136**, 1694–1697.
50 X.-W. Song, H.-M. Wen, C.-B. Ma, H.-H. Cui, H. Chen and C.-N. Chen, *RSC Adv.*, 2014, **4**, 18853–18861.
51 T. Nann, S. K. Ibrahim, P.-M. Woi, S. Xu, J. Ziegler and C. J. Pickett, *Angew. Chem. Int. Ed.*, 2010, **49**, 1574–1577.
52 B. Liu, J. Li, H.-L. Wu, W.-Q. Liu, X. Jiang, Z.-J. Li, B. Chen, C.-H. Tung and L.-Z. Wu, *ACS Appl. Mater. Interfaces*, 2016, **8**, 18577–18583.
53 S. J. Horsewill, G. Hierlmeier, Z. Farasat, J. P. Barham and D. J. Scott, *ACS Catal.*, 2023, **13**, 9392–9403.
54 C. Wan, Y. Ling, S. Wang, H. Pu, Y. Huang and X. Duan, *ACS Cent. Sci.*, 2024, **10**, 658–665.
55 Mounesh, B. A. Thippeswamy, P. Shiralkar, R. Geetha Balakrishna, B. M. Nagaraja and K. Pramoda, *ACS Appl. Energy Mater.*, 2025, **8**, 51–63.
56 Y. Gao, S.-J. Wang, Z. Guo, Y.-Z. Wang, Y.-P. Qu and P.-H. Zhao, *J. Inorg. Biochem.*, 2024, **259**, 112665.
57 R. Wang, X. Sun and B. Han, *Inorg. Chem. Front.*, 2025, **12**, 6926–6945.
58 J. Xian, S. Li, H. Su, P. Liao, S. Wang, Y. Zhang, W. Yang, J. Yang, Y. Sun, Y. Jia, Q. Liu and G. Li, *Angew. Chem., Int. Ed.*, 2023, **62**, e202304007.
59 P. Liao, J. Kang, R. Xiang, S. Wang and G. Li, *Angew. Chem., Int. Ed.*, 2024, **63**, e202311752.
60 T. You, J. Li, S. Bo, W. Yang, H. Sun, Q. Liu, G. Li and L.-Z. Wu, *Angew. Chem., Int. Ed.*, 2026, **65**, e8486876.

View Article Online
DOI: 10.1039/D6TA02884E

All data supporting this study are provided within the article, the Electronic Supplementary Information (ESI), and the accompanying Supplementary Dataset package.

The Supplementary Dataset includes the following components:

(1) Section-wise datasets (CSV files)

- S1.csv (catalyst identity, reaction assignment, anchoring classification)
- S2.csv (reported electrochemical parameters and reaction conditions)
- S3.csv (mechanistic weight assignments: OA, MLC, PCET)
- S4.csv and S4_extracted_from_Explanation.csv (utility and limitation descriptors: U1–U4, R1–R4)
- S5.csv (evidence completeness scores and composite ECOMP)
- S6.csv (experimental regime descriptors: base, solvent, illumination)
- S7.csv (fully integrated dataset used to construct the U–R landscape)

(2) Derived analysis and validation files

- S8 enrichment outputs (enrichment_values.py, enrichment_run_stdout.txt)
- S9 robustness analysis (order_tier_perturbation_analysis.py, README_order_raw_perturbation.txt)
- S10 forward validation files (forward_validation_ccr_scores_forward.csv, forward_validation_md_ccr_cards.txt, forward_projection_report.py)
- S11 statistical analysis outputs (S11_outputs.txt, S11_performance_divergence.py)
- S12 manuscript-level statistical files (manuscript stats report S7.txt, manuscript_statistics.py)
- S13 Circularity sensitivity check (circularity_sensitivity_report.txt, circularity_sensitivity_check.py, circularity_sensitivity_summary.csv, S7_no_S3_quadrant_check.csv)

(3) Descriptor definitions, extraction rules, and integrity summaries

- Section-specific rule documents (e.g., S1_identity_and_anchoring_rules.txt, S3_mechanistic_weighting_rules.txt, S4_utility_and_limitation_rules.txt, S5_design_evidence_composition_rules.txt, S6_experimental_regime_rules.txt)
- Data integrity and composition summaries for S1–S7
- Supporting clarification and robustness files (anchoring_support_clarification.csv, descriptor_separation_logic.csv, UR_robustness_check.csv)

(4) Source data for all figures

- SourceData_Figure_2a–2e, 3a, 3d, 4b, 4e, 5f, 6a–6c
- SourceData_Figure_S1a–S7f and S10b (including S7d_bins.csv for histogram binning)

(5) Offline visualization tool

- CCR_Viewer.html (self-contained browser-based viewer for catalyst-level inspection, including structures, descriptors, and analysis outputs)

All datasets were compiled from publicly available literature sources cited in the manuscript. Descriptor assignments were generated using fixed rule-based extraction protocols, and all derived quantities (e.g., Sum_U, Sum_R, Order Index) were computed using the provided scripts. No new experimental or crystallographic data were generated in this work.